The Instrument of the Imaging X-Ray Polarimetry Explorer

Paolo Soffitta[1], Luca Baldini[2,3], Ronaldo Bellazzini[3], Enrico Costa[1], Luca Latronico[4], Fabio Muleri[1],
Ettore Del Monte[1], Sergio Fabiani[1], Massimo Minuti[3], Michele Pinchera[3], Carmelo Sgro'[3], Gloria Spandre[3], Alessio Trois[5],
Fabrizio Amici[1], Hans Andersson[6], Primo Attina'[7], Matteo Bachetti[5], Mattia Barbanera[3], Fabio Borotto[4], Alessandro Brez[3],
Daniele Brienza[1], Ciro Caporale[4], Claudia Cardelli[3], Rita Carpentiero[8], Simone Castellano[3], Marco Castronuovo[8],
Luca Cavalli[9], Elisabetta Cavazzuti[8], Marco Ceccanti[3], Mauro Centrone[10], Stefano Ciprini[11,12], Saverio Citraro[3],
Fabio D'Amico[8], Elisa D'Alba[9], Sergio Di Cosimo[1], Niccolo' Di Lalla[13], Alessandro Di Marco[1], Giuseppe Di Persio[1],
Immacolata Donnarumma[8], Yuri Evangelista[1], Riccardo Ferrazzoli[1], Asami Hayato[14], Takao Kitaguchi[14], Fabio La Monaca[1],
Carlo Lefevre[1], Pasqualino Loffredo[1], Paolo Lorenzi[9], Leonardo Lucchesi[3], Carlo Magazzu[3], Simone Maldera[4],
Alberto Manfreda[3], Elio Mangraviti[9], Marco Marengo[4], Giorgio Matt[15], Paolo Mereu[4], Alfredo Morbidini[1], Federico Mosti[4],
Toshio Nakano[14], Hikmat Nasimi[1], Barbara Negri[8], Seppo Nenonen[6], Alessio Nuti[3], Leonardo Orsini[3], Matteo Perri[10],
Melissa Pesce-Rollins[3], Raffaele Piazzolla[1], Maura Pilia[5], Alessandro Profeti[3], Simonetta Puccetti[8], John Rankin[1],
Ajay Ratheesh[1,16], Alda Rubini[1], Francesco Santoli[1], Paolo Sarra[9], Emanuele Scalise[1], Andrea Sciortino[9], Toru Tamagawa[14],
Marcello Tardiola[4], Antonino Tobia[1], Marco Vimercati[9], and Fei Xie[1]

[1] Istituto di Astrofisica e Planetologia Spaziali, Via del Fosso del Cavaliere 100, 00133 Rome, Italy; paolo.soffitta@inaf.it
[2] Universita' di Pisa, Lungarno Pacinotti 43, 56126 Pisa, Italy
[3] Istituto Nazionale di Fisica Nucleare, Largo B. Pontecorvo 3, 56127 Pisa, Italy
[4] Istituto Nazionale di Fisica Nucleare, Via P. Giuria 1, 10125 Turin, Italy
[5] Osservatorio Astronomico di Cagliari, Via della Scienza 5, 09047 Selargius (Ca) Italy
[6] Oxford Instruments Technologies Oy, Technopolis Innopoli 1, Tekniikantie 12, FI-02150 Espoo, Finland
[7] Osservatorio Astrofisico di Torino Via Osservatorio, 20, 10025 Pino Torinese (Turin), Italy
[8] Agenzia Spaziale Italiana Via del Politecnico snc, 00133 Rome, Italy
[9] Orbitale Hochtechnologie Bremen, OHB Italia, Via Gallarate 150, 20151 Milan Italy
[10] Osservtorio Astronomico di Rome, Via Frascati 33, 00078 Monte Porzio Catone (Rome) Italy
[11] Istituto Nazionale di Fisica Nucleare (INFN) Sezione di Rome Tor Vergata, Via della Ricerca Scientifica 1, 00133 Rome, Italy
[12] Agenzia Spaziale Italiana Space Science Data Center (SSDC) Via del Politecnico snc, 00133 Rome, Italy
[13] W.W. Hansen Experimental Physics Laboratory, Kavli Institute for Particle Astro-physics and Cosmology, Department of Physics and SLAC National Accelerator Laboratory, Stanford University, Stanford, CA 94305, USA
[14] RIKEN Nishina Center, 2-1 Hirosawa, Wako, Saitama 351-0198, Japan
[15] Dipartimento di Matematica e Fisica, Universita' degli Studi Rome Tre, Via della Vasca Navale 84, 00146 Rome, Italy
[16] Dipartimento Di Fisica Universita' degli Studi di Rome "Tor Vergata," Via della Ricerca Scientifica 1, 00133 Rome, Italy

Abstract

While X-ray spectroscopy, timing, and imaging have improved much since 1962 when the first astronomical nonsolar source was discovered, especially wi the launch of the Newton/X-ray Multi-Mirror Mission, Rossi/X-ray Timing Explorer, and Chandra/Advanced X-ray Astrophysics Facility, the progress of X-ray polarimetry has been meager. This is in part due to the lack of sensitive polarization detectors, which in turn is a result of the fate of approved missions and because celestial X-ray sources appear less polarized than expected. Only one positive measurement has been available until now: the Orbiting Solar Observatory measured the polarization of the Crab Nebula in the 1970s. The advent of microelectronics techniques has allowed for designing a detector based on the photoelectric effect of gas in an energy range where the optics are efficient at focusing in X-rays. Here we describe the instrument, which is the major contribution of the Italian collaboration to the Small Explorer mission called IXPE, the Imaging X-ray Polarimetry Explorer, which will launch in late 2021. The instrument is composed of three detector units based on this technique and a detector service unit. Three mirror modules provided by Marshall Space Flight Center focus X-rays onto the detectors. We show the technological choices, their scientific motivation, and results from the calibration of the instrument. IXPE will perform imaging, timing, and energy-resolved polarimetry in the 2–8 keV energy band opening this window of X-ray astronomy to tens of celestial sources of almost all classes.

Unified Astronomy Thesaurus concepts: X-ray astronomy (1810); X-ray detectors (1815); Polarimetry (1278)

1. Introduction

Historically, since the dawn of X-ray astronomy, polarimetry was considered a "holy grail" due to the characteristics of the radiation emitted by the celestial sources and their typically nonspherical geometry. Rockets flown in the late 1960s (Angel et al. 1969) and early 1970s (Novick et al. 1972) had polarimeters based on the "classical" techniques of Bragg diffraction (Schnopper & Kalata 1969) and Thomson scattering (Angel et al. 1969). A rocket experiment in the 1970s hinted at polarized emission from the Crab Nebula and Pulsar (Novick et al. 1972). The eight Orbiting Solar Observatory (OSO-8) X-ray polarimeters confirmed this result with a much higher significance ($\Pi = 19.2\% \pm 1.0\%$ @ 2.6 keV, Weisskopf et al. 1978b), definitively establishing the synchrotron origin of the nebular X-ray emission. Due to its limited observing time and relatively high background, the OSO-8 X-ray Bragg polarimeter obtained useful upper limits for just a few other
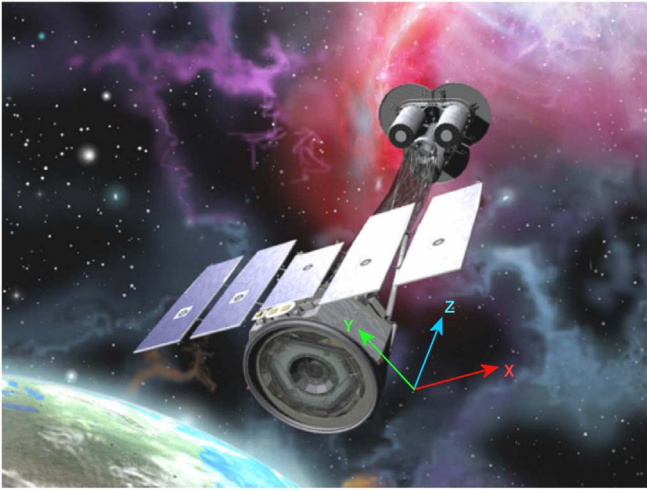
Figure 1. The Imaging X-ray Polarimetry Explorer with its three detector units at the focus of the three mirror modules.

bright galactic X-ray sources, while for many others the upper limits were too coarse to constrain models (Weisskopf et al. 1977, 1978a; Hughes et al. 1984). From the advent of X-ray telescopes starting with the Einstein satellite, it was clear that a quantum leap required a focal-plane instrument. An experiment based on the classical techniques was devised and built but never flown (Kaaret et al. 1989; Soffitta et al. 1998; Tomsick et al. 1997).

An experiment tuned to the classical energy band of X-ray astronomy (2–8 keV for the IXPE) allows for meaningful polarimetry of basically all classes of celestial sources with, maybe, the exception of clusters of galaxies. To be effective in this energy band, polarimetry must be based on the photo-electric effect, a long-sought method by means of which it is also possible to derive the impact point, the energy, and time with suitable devices (Heitler 1954; Sanford et al. 1970; Soffitta et al. 2001). Classical methods like Bragg diffraction (Schnopper & Kalata 1969; Novick et al. 1972) are effective only in one or two narrow energy bands or, like Thomson scattering, (Angel et al. 1969) suffer from high background and high energy threshold. The band, the modulation factor (see Section 2), and the efficiency of a photoemission polarimeter required a complex trade-off in the choice of the gas mixture, of its pressure, and of the detector drift length. This was the result of years of extended simulations and measurements (Muleri et al. 2008a, 2010).

The advent of techniques typical of microelectronics allowed us to build sensitive polarimeters with imaging capabilities (Costa et al. 2001; Bellazzini et al. 2006, 2007). Later, nonimaging polarimeters with large quantum efficiency (Black et al. 2007) but requiring rotation due to spurious effects intrinsic to the readout methodology, were also devised. The Gravity and Extreme Magnetism SMEX (Small Explorer; Swank 2010) based on the latter technology was eventually selected but then canceled in 2012 for programmatic reasons. A mission similar to IXPE was proposed as a small ESA mission (Soffitta et al. 2013b) and then, redesigned, as MIDEX ESA mission down-selected for competitive phase A but not approved for flight (Soffitta & XIPE Collaboration 2017). IXPE (Weisskopf et al. 2008, 2016), see Figure 1, is a SMEX scientific mission selected by NASA in 2017 January with a large contribution from Agenzia Spaziale Italiana (ASI) to be launched in 2021 aboard a SpaceX Falcon-9 rocket. It will

measure polarization in X-rays from neutron stars, from stellar-mass black holes, and from active galactic nuclei (AGNs). For the brightest extended sources like pulsar wind nebulae (PWNe), supernova remnants (SNRs), and large-scale jets in AGNs, IXPE will perform angularly resolved polarimetry. In some cases, IXPE will definitively answer important questions about source geometry and emission mechanisms or even exotic effects in extreme environments. In others, it will provide useful constraints including the possibility that no currently proposed model explains the data.

A gas pixel detector (GPD), based on the same technology exploited in IXPE (Baldini et al. 2021), was flown onboard a CubeSat and is, presently, collecting scientific data from a long observation of the Crab Nebula with a possible detection of a time variation of polarization of the pulsar (Feng et al. 2020) and other bright sources.

The sensitivity of IXPE is 30 times better than that of the Bragg polarimeter onboard OSO-8 for a 10 mCrab source, while it is more then two orders of magnitude better then the GPD onboard the Cubesat for a source of the same intensity. While polarimetry of AGNs was precluded to OSO-8, it is within the reach of IXPE which also provides imaging capability in combination with simultaneous spectral and temporal measurements. IXPE's design is based on the scientific requirements summarized in Table 1.

A characteristic of IXPE is the dithering during observations. This has been introduced to avoid having to calibrate pixel by pixel as with Chandra and other observatories with imaging detectors (see Section 6.2). Modern X-ray telescope missions are designed for staring or dithering observations. Each detector is mounted with respect to the next one on the top deck of the spacecraft with an angle around the Z axis, (the axis of the incoming photon beam; see Figure 1) of 120°. Such a disposition allows for a sensitive reduction and checks for spurious effects.

2. The Statistics for an Experiment of Polarimetry

A detector system can measure polarization if its response is modulated by the polarization of the incoming photons. The photoelectric effect modulates the emission direction of an s-photoelectron as $\cos^2$ of the azimuthal angle, which is the emission angle with respect to the polarization angle. This $\cos^2$ dependence is a general feature for a polarimeter. The modulation curve is the angular distribution of the emission directions of photoelectrons in our case and the peak positions determine the polarization angle. The amplitude of the modulation is defined as the semi-amplitude of the modulation curves normalized to its average. If the incoming radiation is 100% polarized, the modulation amplitude is the so-called modulation factor μ. This is a key parameter of a polarimeter and spans from 0, if the instrument is not sensitive to polarization, to 1, in the case of an ideal polarimeter.

The sensitivity of a polarimeter is expressed in terms of minimum detectable polarization ($\mathrm{MDP_{CL}}$) where CL is the confidence level:

$$\mathrm{MDP_{CL}} = \sqrt{-2\ln(1-\mathrm{CL})} \times \frac{\sqrt{2(C_S + C_B)}}{\mu \times C_S}$$
$$= \sqrt{-2\ln(1-\mathrm{CL})} \times \sigma_P. \tag{1}$$

Table 1
IXPE Scientific Requirements

Physical Parameter	Observable	Property	Value
Linear Polarization	Degree Π, angle ψ	Sensitivity $\mathrm{MDP}_{99}(F_{2\text{–}8} = 10^{-11}$ cgs, $\Delta t = 10$ days)	$\leqslant 5.5\%$
		Systematic error in polarization degree Π(5.9 keV)	$\leqslant 0.3\%$
		Systematic error in position angle ψ (6.4 keV)	$\leqslant 1°$
Energy dependence	$F(E)$, $\Pi(E)$, $\psi(E)$	Energy band $E_{\min}$–$E_{\max}$	2–8 keV
		Energy resolution $\Delta E(E = 5.9$ keV$)$, $\propto \sqrt{E}$	$\leqslant 1.5$ keV
Spatial dependence	$F(k)$, $\Pi(k)$, $\psi(k)$	Angular resolution HPD (system-level)	$\leqslant 30''$
		FOV $\gg$ HPD	$\geqslant 9'$
Time dependence	$F(t)$, $\Pi(t)$, $\psi(t)$	Time accuracy $<<$ source pulse periods	$\leqslant 0.25$ ms
Areal background rate	R_B/A_{det}	$R_B/A_{\mathrm{det}} << R_S/A_S$ for faint source (2–8 keV, per DU)	< 0.004 s^{-1} cm^{-2}

Note. Half-power diameter (HPD), field of view (FOV), and minimum detectable polarization (MDP) are shown.

C_S are the total source counts, and C_B are the total background counts. We usually set $\mathrm{CL} = 0.99$ to get the MDP_{99} and we get:

$$\mathrm{MDP}_{99} = 4.29 \times \frac{\sqrt{C_S + C_B}}{\mu \times C_S} \qquad (2)$$

$$\mathrm{MDA}_{99} = 4.29 \times \frac{\sqrt{C_S + C_B}}{C_S}. \qquad (3)$$

The minimum detectable amplitude is the minimum modulated signal measurable from a polarized source at 99% confidence level. It consists of the MDP not normalized by the instrumental modulation factor μ. The raw measurement, indeed, consists of a histogram of photoelectron emission directions (the so-called modulation curve) modulated by the X-ray polarization of the incoming beam.

If a polarization is detected with a modulation amplitude equal to MDA_{99}, the measurement is only at about the 3σ (Elsner et al. 2012):

$$n_\sigma = \sqrt{-2 \times \ln(1 - \mathrm{CL})} = 3.03. \qquad (4)$$

Sadly, X-ray polarimetry is possible only for relatively bright celestial sources due to the large number of counts needed to build the modulation curve. For focal-plane polarimeters, the background in case of an observation of a point-like source consists only of un-rejected events located within the point-spread function of the optics. As a matter of fact, for these two reasons, the background for all the point-like celestial sources suitable for polarimetry is negligible (Xie et al. 2021). Therefore, the sensitivity in this case depends inversely on μ and the square root of the total source counts. In turn, the total number of the source counts depends linearly on the observing time T, mirror effective area A_{eff}, efficiency of the detector ϵ, and the source spectrum S. In this case, the minimum detectable polarization (MDP) can be expressed as:

$$\mathrm{MDP}_{99} = \frac{4.29}{\mu\sqrt{S A_{\mathrm{eff}} \, \epsilon \, T}}. \qquad (5)$$

The quality factor of the detector can be expressed as $\mathrm{QF} = \mu \times \sqrt{\epsilon}$. A trade-off between μ and ϵ provides the best sensitivity to polarization obtainable by the detector.

We also use the Stokes parameters to characterize the polarization. These have the advantage that, as opposed to the degree of polarization and the position angle, they are statistically independent. According to the prescription in Kislat et al. (2015) we calculated the Stokes parameters of each count. We sum up the corresponding Stokes parameter to determine the polarization degree and polarization angle of the beam. By fitting a cosine function or summing the Stokes parameter, we obtain the same results.

3. The Scientific Drivers of the Instrument

IXPE scientific requirements descend from the expected polarization properties of the celestial sources and their temporal, spectral, and spatial characteristics. The sensitivity of IXPE, as shown in Table 1, is set for meaningful polarimetry with a realistic observing time of the brightest AGNs. The residual systematic error in the modulation amplitude should allow for polarimetry below 1% when observing bright galactic sources. The requirement on the systematics of the polarization angle allows us to check possible variation with respect to the old OSO-8 polarimetry of the Crab Nebula. Also, it allows for an effective comparison, at different wavelengths, of phase-resolved X-ray polarimetry in combination with the requirement on the timing accuracy. The requirement on angular resolution is derived by the capability to angularly separate the central pulsar from the surrounding torus in the Crab Pulsar Wind Nebula.

Table 2 breaks down the scientific requirements into instrument requirements. As a matter of fact, polarization sensitivity depends inversely on the modulation factor and the inverse of the square root of the quantum efficiency. The requirement on the modulation factor is more stringent with respect to the quantum efficiency. As a matter of fact, a deficit in quantum efficiency results in a linear increase of the observing time to get the same sensitivity. A deficit in the modulation factor requires, instead, a quadratic increment.

The requirement on the maximum allowed modulation amplitude from an unpolarized source was set, initially, only at 5.9 keV because of the availability of a true unpolarized

Table 2
IXPE Instrument Requirements

Parameter	Requirement
Modulation factor	>27.7 at 2.6 keV (with 20% cut)
Modulation factor	>53.7 at 6.4 keV (with 20% cut)
Spurious modulation	<0.27% at 5.9 keV
GPD quantum efficiency	>17.7% at 2.6 keV
GPD quantum efficiency	>1.8% at 6.4 keV
Energy resolution	1.5 keV (at 5.9 keV)
Knowledge of the spurious modulation	<0.1% at 2–8 keV keV
Systematic error on angle	<0.4 deg
Position resolution (HPD)	<190 μm at 2.3 keV
Dead time	<1.2 ms (average at 3 keV)
Maximum counting rate	900 c/s
Time accuracy	$\pm$ 94 μs (99%)
Background	<0.004 s^{-1} cm^{-2} per DU (2–8 keV)

Note. Where indicated, the 20% cuts refer to an optimum selection of the data (see, for example, Section 2) that maximizes the sensitivity considering the events with the most elongated tracks.

source. A low energy effect (see Section 6.2) was found and characterized.

Time resolution and time accuracy requirements are set according to what the technology offers thanks to the use of a GPS receiver with a large discovery space in case of pulsating neutron stars either isolated or in binary systems.

The largest contribution to the angular resolution of the telescope system is the HPD of the mirror (Fabiani et al. 2014). The second contribution is the inclined penetration of X-rays onto the detector which has an active volume with 1cm deep thickness. The third contribution is the position resolution of the detectors which is negligible with respect to the other two. The requirement on the blurring (position resolution) of the detector in Table 2 is set not to spoil the angular resolution of the telescope by more than a few percent.

The detector has been designed with sufficient FOV when coupled with mirrors having a focal length of a few meters. With such a focal length, mirrors are efficient for reflecting X-rays in the classical 1–10 keV energy band. The FOV requirement allows for polarimetry with a single observation of shell-like supernovae like Cas A, Tycho, and Kepler (Soffitta et al. 2013a).

The energy resolution requirement allows for studying energy-dependent phenomena, like, for example, the energy-dependent rotation of the polarization angle in galactic black hole binaries in the thermal state (Connors & Stark 1977; Stark & Connors 1977). Moreover, this requirement allows us to assign the correct modulation factor, rapidly increasing with energy, to the detected photons, deriving the polarization of the X-ray sources.

A small dead time allows for a minimum decrement of the detected counting rate and therefore, of the sensitivity, from sources as bright as the Crab Nebula. Due to the limitation of the onboard memory and the requirement of the use of the S band for on-ground data transmission, particular care must be taken to interleave bright source observations with faint source observations.

The background-rate requirement, albeit larger than that of space experiments with gas detectors with front and rear anti-coincidence, allows for measuring polarization from dim and extended sources like molecular clouds in the galactic center region.

4. IXPE Payload Overview

The IXPE payload (O'Dell et al. 2018, 2019; Soffitta et al. 2020) consists of a set of three identical telescope systems co-aligned to the pointing axis of the spacecraft and with star trackers. Each system, while operating independently, comprises a 4 m focal length mirror module assembly (MMA, Ramsey et al. 2019) that focuses X-rays onto the respective detector units (DUs). Each DU hosts one polarization-sensitive imaging detector with its own electronics, which communicates with a detector service unit (DSU) interfaced to the spacecraft's integrated avionics unit (IAU). The three DUs and the DSU are collectively called the IXPE Instrument. The DUs are mechanically mounted onto the top deck of the spacecraft oriented, as already mentioned, with a rotation of 120° each with respect to the beam axis (Z axis; see Figure 1).

The performance of the detectors and, particularly, the gain, have to be monitored during the operative life of the mission. Other parameters, like the modulation factor, are expected, from ground calibration, to be more stable in time but they can be monitored as well. For these reasons, each DU is equipped with a multi-function filter and calibration wheel assembly that allows for (i) in-flight calibration of the modulation factor, (ii) the calibration of the gain, (iii) source-flux attenuation, and (iv) background measurements. MMA and DUs are separated by deployable (3.5 m) boom; the position of the MMA with respect to the DUs can be adjusted after deployment with a tip/tilt/rotate mechanism. Each MMA hosts an X-ray shield to avoid, in combination with a stray-light collimator mounted onto the top of the DU, X-ray photons impinging on the detector active area when arriving from outside the telescope field of view. The use of a set of telescopes provides many advantages with respect to a configuration based on a single telescope of equivalent collecting area. First of all, since the energy bandpass fixes the ratio between the mirror diameter and the focal length, a multiple telescope configuration is more compact than a single larger telescope; this occurs at the cost of an increase of the measured background which, however, is not a driving requirement for IXPE. Moreover, a multiple system is intrinsically redundant and offers the possibility of comparing independent data and correcting small effects which may mimic a real signal.

5. The Design of the Instrument

The design of the instrument, and in particular, the design of the DUs, is the consequence of the prescription of using the Pegasus XL launcher at the time of the proposal. The top deck of the spacecraft hosts at launch both the three un-deployed mirrors and the three DUs. Hence, the available space in the top deck requires a vertically stacked mechanical configuration for the DUs. Such a configuration is demanding in terms of thermal dissipation and, in addition, has a worse response to vibrations than a side-by-side configuration. In the following phase of competitive bidding during phase B, a Falcon-9 was eventually selected and will lift IXPE to the foreseen 600 km equatorial orbit.

The IXPE Instrument, mainly supported by the Italian Space Agency, ASI, has been entirely designed, built, and tested in Italy. We show the items of the instrument as the Italian IXPE
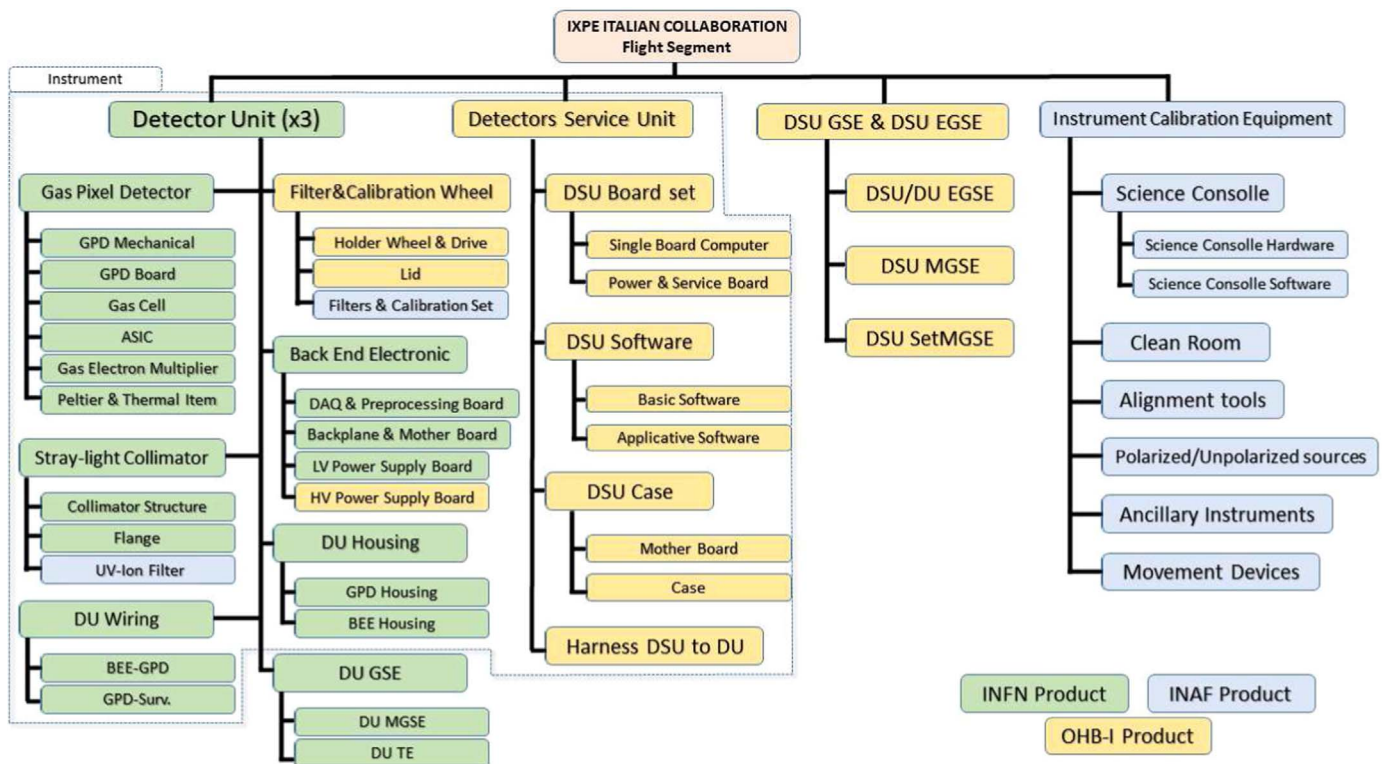
Figure 2. Instrument product tree.

contribution in Figure 2. In the same figure, the responsibilities for each item that are shared between INAF, INFN, and the industrial partner OHB-Italy are shown.

Each of the four DUs (including one spare unit; see Figure 3), comprises the following sub-units:

1. Gas pixel detector (GPD), which is an X-ray detector with gas as the absorption medium and an application-specific integrated circuit (ASIC) as the readout electrode, specifically developed by INFN in collaboration with INAF-IAPS for X-ray polarimetry.
2. Filter and calibration wheel (FCW), which hosts the calibration set comprising calibration sources and filters for specific observations to be placed in front of the GPD when needed.
3. Back-end electronics (BEE), which comprise electronics boards (DAQ, data acquisition board, Barbanera et al. (2021) to manage the GPD ASIC), the required high-voltage lines, and the low-voltages lines.
4. Stray-light collimator (STC), already mentioned above.
5. DU housing (DUH), which provides the mechanical and thermal interface of the DU to the S/C.
6. DU wiring (DUW), which provides the electrical interfaces (internal to the DU) between the BEE and the GPD.

The DSU is the unit that provides the DU with the needed secondary power lines and controls and powers the FCW, formats, and forwards the scientific data of the three DUs to the spacecraft. The DSU comprises the following sub-units.

1. DSU board set (DBS), which is the set of electronic boards (both nominal and redundant) that perform the DSU tasks.

2. DSU software, which comprises the software that runs in the DSU.
3. DSU case (DSC), which includes a backplane that provides the electrical interface among the DSU boards. Further, the DSU case provides the mechanical and thermal interface of the unit.
4. Harness DSU to DU, which comprises the cables necessary to electrically interface the three DUs to the DSU.

Moreover, to complete the instrument-related units, two testing/calibration stations were assembled. One is the instrument calibration equipment, which is briefly described in Section 9, and the companion assembly verification and test equipment. The latter has three positions, one for each DU. Each testing/calibration station consist of X-ray sources, collimators, crystals, and computer-controlled stages to calibrate the DUs and to perform the bench integration of the instrument. The electrical ground support equipment has also been assembled to manage the DUs and DSU calibration activities and bench integration.

In this paper we present the status of the instrument before assembly with the spacecraft. However, due to its design, any change of performance after the integration is not expected.

6. The IXPE Detector Unit

In order to save space, the DUs were designed with a top to bottom configuration for the detector and associated electronics, respectively. The 120° clocking allows for checking the level of absence of spurious modulation and limiting any systematic effects. An expanded view of the DU and a picture of an assembled DU are shown in Figure 3.
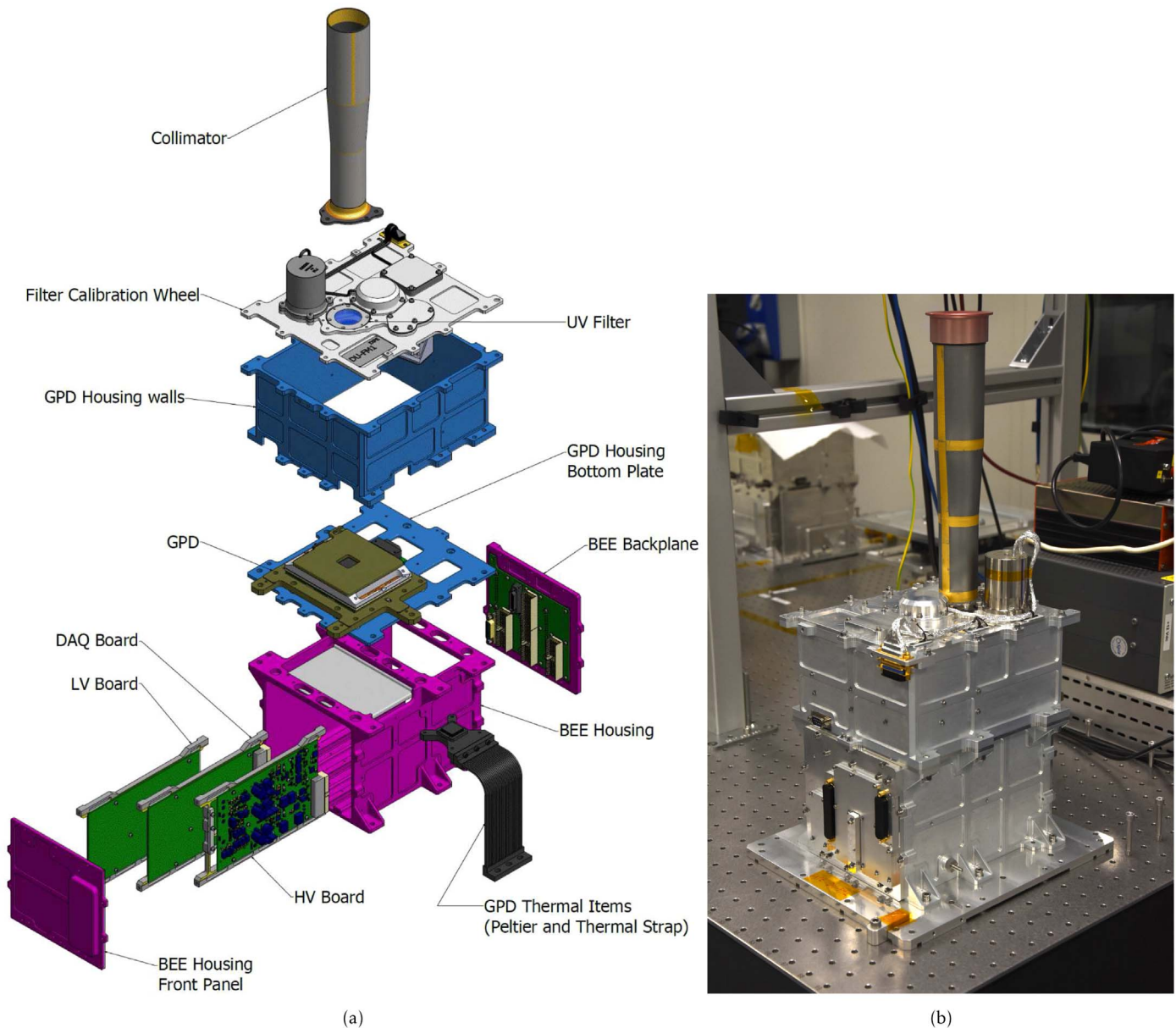
Figure 3. The IXPE detector units (a) expanded view of a detector unit and (b) photograph of a flight detector unit in its handling plane. The thermal environment is controlled by means of a Peltier cooler and a heater. A thermal strap conducts the heat from the GPD Peltier/heater system to the radiator of the spacecraft.

The DU housing is composed of two boxes. The top one is the "GPD housing." The bottom item is the "back-end housing." In the next sections we describe the main elements of the DUs.

6.1. Stray-light Collimator and UV-ion Filter

An extensible boom connects the mirror modules to the spacecraft top deck. This open-sky configuration requires a system to prevent cosmic X-ray background photons from outside the mirror field of view from impinging on the detector. To this aim, a tapered stray-light carbon-fiber (CF) collimator collects only the photons reflected by the optics, thanks also to fixed X-ray shields around the mirror modules. The thickness of the collimator is 1.25 mm and includes a 1 mm thick CF with an external 50 μm molybdenum coating and 20 μm gold of the molybdenum foil.

Due to the fact that the beryllium window of the detector and the supporting titanium frame is at high potential (about −2800 V), positive ions may interact with the top GPD structure, producing eventual secondary photons and a possible failure of the high-voltage system. For this reason, photons from the optics cross a UV-ion filter made by LUXEL composed of 1059 nm of LuxFilm® (based on kapton) with an external coating of 50 nm of aluminum and an internal coating of 5 nm of carbon. The UV-ion filters are described in La Monaca et al. (2021). The scope of the UV-ion filter is to prevent UVs and low-velocity plasma present in the orbit from reaching the beryllium window of the GPD (see Section 6.2). The transparencies at two energies are reported in Table 5.

6.2. The Gas Pixel Detector in the Detector Unit

The GPD (see Figure 4), located in the GPD housing, is a gas detector for which the charge-signal is read out by a matrix
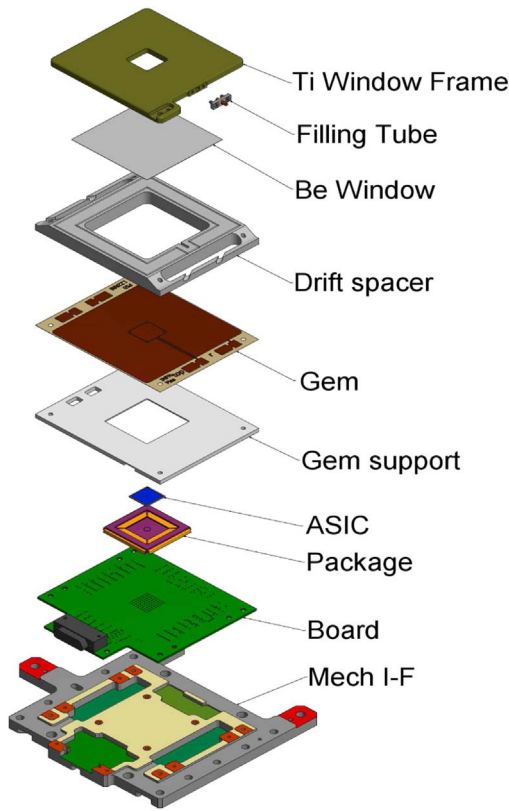
3. Ceramic spacer (GEM support frame), supporting and insulating the GEM from the GPD board; the lower gas gap of 770 μm for the drift of the amplified electrons is defined by the ASIC top surface and the bottom GEM.
4. The GEM foil (GEM), including four soldering pads for the high-voltage connections.
5. Ceramic support (drift spacer), which defines the absorption gas cell above the GEM and isolates the GEM from the top electrode.
6. Titanium frame (Ti frame and Be window) which closes the gas cell and allows X-rays into the GPD through the integrated thin, optical-grade 50 μm single-side aluminized beryllium window. The titanium frame and the beryllium window also serve as a drift electrode.
7. Filling tube of oxygen-free high-conductivity copper and its fixture to the titanium frame (tube and fixture).

The GPD is sealed and does not require any gas-cycling systems. The keystone of the assembly is the Kyocera package. In fact, the ASIC is designed to fit into a commercial package that acts as the bottom parts of the gas cell and connects the internal wiring and the clean gas volume to the external printed circuit board (PCB), onto which the package is soldered. In this way, cleanness is preserved in the gas volume.

The GPD assembly is done at INFN, whereas the filling procedure is performed at Oxford Instruments Technologies Oy (OIT, Espoo, Finland). After a vacuum leak-tightness check, the GPD is continuously baked-out and pumped-down for 14 days at 100 °C for outgassing and eliminating possible impurities in the internal gas cell. Finally, the GPD is filled with a dimethyl ether (DME) mixture at 800 mbar at room temperature. OIT filled with the same gas mixture, a single-wire proportional connected in parallel to the same filling station to check the energy resolution. If the energy resolution is within the requirement, the filling tube of the GPD is crimped. We selected this three-times distilled gas mixture because it minimizes track blurring thanks to its small transverse diffusion ($\frac{69\ \mu\mathrm{m}}{\sqrt{\mathrm{cm}}}$ at 1833 V cm^{-1} and 0.8 bar). Its pressure is optimized in order to provide the best combination of efficiency and modulation factor and, therefore, the sensitivity in the energy range of interest. Indeed a lower pressure increases the track length, but also the diffusion and reduces the quantum efficiency. A larger pressure, instead, increases the quantum efficiency but reduces the track length and this reduction is not compensated in terms of modulation factor by the simultaneous reduction of diffusion. In Section 7.1 we will describe a peculiar phenomenon called "virtual leak" that reduces asymptotically the pressure at 640–650 millibar increasing the track length.

Three negative high voltages are required by the GPD. The GEM bottom voltage (V_{bottom} on the side facing the ASIC) sets the electric field in the transfer gap between the GEM and the ASIC. The difference between the GEM top voltages (V_{top} on the side facing the window) and V_{bottom} sets the gas gain. The high voltage on the titanium frame and beryllium window, (V_{drift}) sets the drift voltage in the absorption region in combination with the V_{top}.

The performance of the GPD is, in principle, dependent on temperature to some extent. The GPD temperature is controlled during the operation by means of a Peltier cooler and heaters. A thermal strap connects the cooler directly to the spacecraft radiator. The GPD thermal control is performed directly by the DSU and is designed to be as independent as possible from the
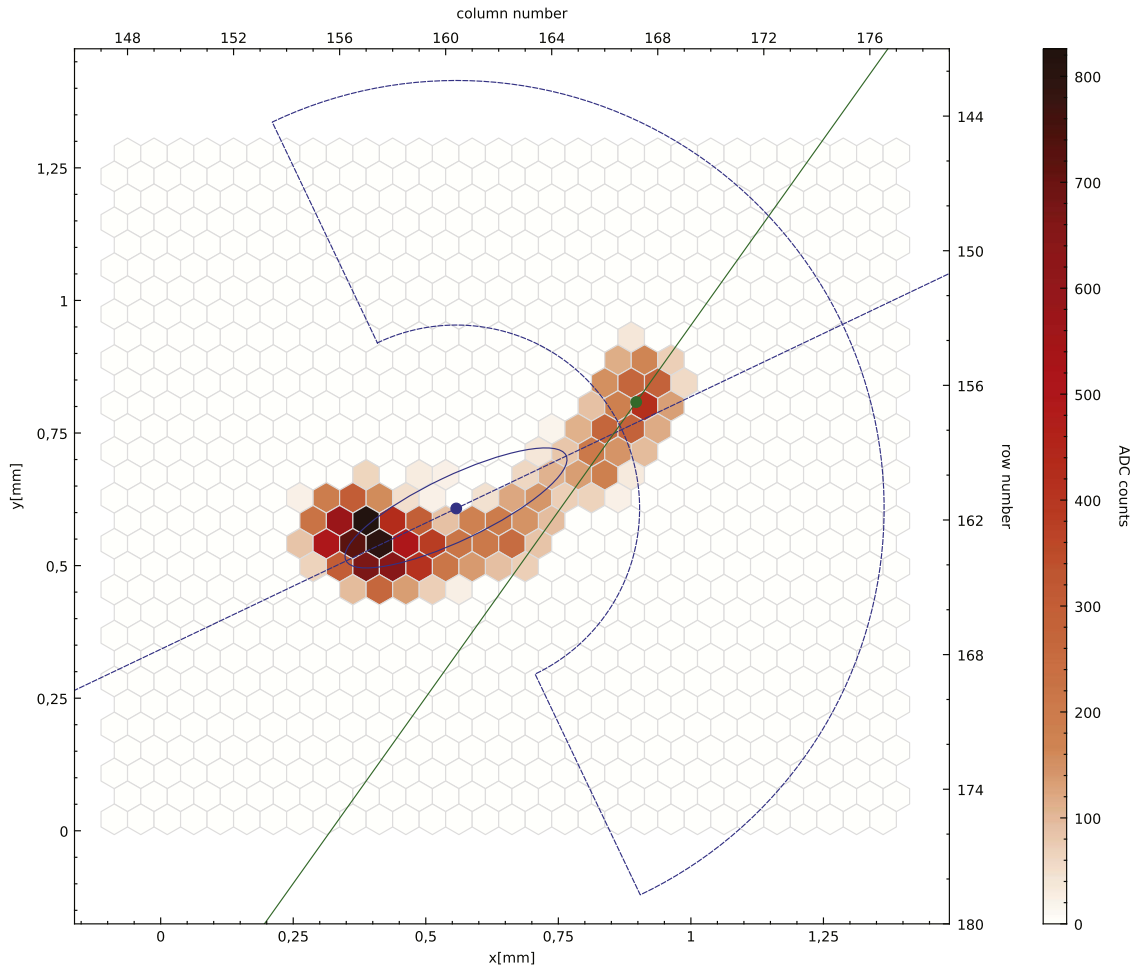

Figure 4. Schematic representation of GPD assembly.

of 105 k pixels (300 × 352 pixels arranged in a 50 μm pitch hexagonal pattern) of a dedicated, custom complementary metal-oxide semiconductor (CMOS) ASIC (Bellazzini et al. 2006). The custom ASIC has self-triggering capabilities thanks to local triggers defining each group of four pixels called mini-clusters. Each event consists of a region of interest (ROI) made by all the mini-clusters that trigger plus a selectable additional fiducial region of 10/20 pixels. The charge content of each pixel in the ROI is readout serially from a single buffer as differential current output by means of a 5 MHz clock. The ASIC also provides the absolute position of the ROI as digital coordinates of two opposite vertices and the global trigger output about 1 μs after the arrival of the charge. The threshold is set low enough to collect signals coming from events that release about 300 eV. The charge amplification is provided by a gas electron multiplier (GEM), a thin 50 μm dielectric (liquid crystal polymer) foil with 9 μm copper metallization on both sides. Through holes are laser-etched and disposed on a regular triangular pattern with vertices 50 μm apart. These cylindrical holes have a diameter of 30 μm (Tamagawa et al. 2009, 2010). The basic building blocks of the GPD assembly and their functions are schematically illustrated in Figure 4. The small pitch of the ASIC and the GEM are responsible for the good image of the photoelectron track (see Figure 5).

In summary, the GPD is composed of the following subassemblies.

1. Mechanical interface (GPD mech. I/F), made of titanium, which supports the GPD unit, connects it to the focal plane, and provides references for alignment with the MMA.
2. Printed circuit board (GPD board), which connects the GPD to the readout electronics.

Figure 5. Real photoelectron track at 5.9 keV with reconstructed direction of emission and absorption point.

BEE temperature since the latter has much looser requirements. The Peltier cooler and the heaters and the thermal dissipation of the spacecraft maintain the temperature of the GPD within the range 15–30 °C.

7. The Physical Quantities Provided by the GPD

Thanks to the GPD, all the information contained in the observed X-ray radiation is provided to the user. After that, a proper algorithm is applied to the data (see Section 11). The projection of the track onto the hexagonally patterned top layer of the ASIC is analyzed to reconstruct the point of impact and the original direction of the photoelectron. The impact point, not the charge barycenter, gives an imaging resolution that is better than 190 μm in diameter (Soffitta et al. 2012). The eventual spatial resolution of the instrument is due to the diffusion of the initial track, to the reconstruction algorithm capabilities, and to the quantization of the GPD pixel size.

The energy is estimated by summing the charge content of each pixel.

The event time is determined by the trigger output of the ASIC. Compared with a charge-coupled device (CCD) currently flying in most of the space mission with X-ray optics, no pile-up issue is present because of the fast drift time (1 cm μs^{-1}) coupled with the fast inhibition to additional charge processed by the ASIC.

The linear polarization is determined by the angular distribution of the emission directions of the photoelectron tracks in the selected energy band. This is called the modulation curve. If the

radiation is polarized, the modulation curve shows a cosine square modulation, whose amplitude is proportional to the degree of polarization and whose phase coincides with the angle of polarization. The amplitude of the modulation of the incident beam is eventually normalized to the modulation obtained for 100% completely polarized photons (the so-called modulation factor μ) to get the beam polarization. The energy-dependent modulation factor of the GPD is measured at different discrete energies during the calibration campaign of the detector and agrees well with predictions derived by accurate Monte Carlo simulations.

During the construction phase of the instrument, and in particular of the gas pixel detector, we detected a nonzero modulation from unpolarized radiation. This signal is called spurious modulation. The amplitude of this signal is of the order of 1.5% on each DU, at 2 keV rapidly declining with energy. The root cause of this spurious modulation is not totally understood yet, but we have identified a few effects that contribute to it by systematically deforming the photoelectron track. Some of them, collectively called "ASIC effects," originate from small systematic biases in the ROI reading. These are typically tiny, i.e., a fraction of the pixel electronic noise in amplitude, yet they cause a measurable effect on large numbers of counts. They were minimized by an appropriate choice of the readout clock frequency and eventually canceled out by subtracting the residual measured bias from the data in the off-line analysis. Another contribution to spurious modulation comes possibly from the

deformation of the track during multiplication, as is suggested by the correlation between the gain spatial mapping and the spurious modulation spatial mapping. In order to subtract the spurious modulation from the data, we organized a vigorous calibration campaign for each DU in such a way as to dedicate most of the time to characterize this effect. We used several nearly unpolarized sources at different energies and on different regions of the detector, from 2 keV up to 5.9 keV where this effect vanishes. More details on the calibration campaign are reported in Section 9.

7.1. Short and Secular Gain Variation

A short-term rate-dependent gain decreasing, accompanied by a secular gain increasing, was also detected. The first one is due to charging effects on the exposed dielectric by drifting ions and electrons during the multiplication process. The second is likely due to an absorption or adsorption of the gas by materials inside the GPD. These two effects have been studied in detail. The first effect is described by simple functions applied by the processing pipeline to the data for gain normalization. The second effect is expected to saturate at an average 640–650 mbar by the time of the flight as indicated by the gain, the counting rate from a ^{55}Fe reference source, and the track length trends. All these parameters are, simultaneously, well modeled in 10 detectors, including the three flight DUs, the spare DU, and the GPD control sample (Baldini et al. 2021). The impact is a decrement of the quantum efficiency, however, the accompanying increase of the modulation factor reduces the loss of sensitivity to an acceptable level.

7.2. The Filters and Calibration Wheel

The filter and the calibration wheel (FCW) have been designed to monitor the performance of the detector during the life of the mission. In particular, we intend to check the low- and high-energy modulation factor and the spurious modulation during the observational life of the mission. Also, we monitor the gain that depends both on temperature and on charging (see Sections 6.2 and 7.1).

The FCW hosts filters to perform special observations (e.g., very bright sources) and calibration sources to monitor detector performance during flight. The FCW has seven positions commanded by the DSU. The positions correspond to open position, closed position, gray filter, and calibration sources A, B, C, and D. The stepper motor is a Phytron phySPACE^{TM} 42-2. It is a COTS component with 25 yr of space flight heritage. The phySPACE^{TM} series is developed and built to resist vacuum, vibrations, low/high temperature, and radiation while maintaining high performance, precise positioning, and long life. The motor pinion is made of Vespel®. The double bearing system that connects the fixed part to the rotating one is made of stainless steel. The positioning is performed and monitored by two different systems.

One system is based on the use of Hall sensors as noncontact switches to stop the wheel rotation at the requested position. A combination of three hall sensors allows for setting and monitoring the seven wheel positions.

In order to have an independent measurement of the wheel position, a second analog device, a Novotechnik PRS65/S152 potentiometer, is implemented. A qualification campaign allowed for declaring this component as flight-compatible.

The FCW positioning can be set digitally or on a step-by-step basis permitting gain and modulation factor to be measured at various positions on the detector.

The calibration set is composed of the X-ray sources and their holders. It comprises the items that can be put in front of the GPD by rotating the FCW. The design of the calibration set is shown in Figure 6.

In the following, we summarize the particular positions which are also described in Ferrazzoli et al. (2020).

1. Open position. The open position is the standard one used for astrophysical observations.
2. Closed position. The closed position has two motivations. It is a safe position for the instrument, but it is also necessary to gather instrumental (internal) background to be compared with that obtainable during Earth occultation.
3. Gray filter. Because of the relatively large (>1 ms) dead time of the gas pixel detector and the available throughput from the bus and from the down-link, we decided to include a partially opaque absorber. This partially opaque absorber is designed to be used when the count rate is greater than that produced by a source about four times more intense than the Crab or greater. It absorbs efficiently low-energy photons where the count rates are greater. At higher energies, where the count rates are smaller, the absorption is small. The filter is made of 75 μm thick kapton foil with 100 nm aluminum on both sides. For a Crab-like spectrum (power law with index 2), the flux will be reduced by a factor of about 6 in the 1–12 keV energy band. The measured energy-dependent transparency is shown in Figure 7.
4. Calibration source A (Cal A). This source produces polarized X-ray photons at two energies (3.0 and 5.9 keV) to monitor the modulation factor of the instrument in the IXPE energy band. An expanded view of this source is shown in Figure 6. A single ^{55}Fe nuclide is mounted and glued into a T-shaped holder. X-rays from ^{55}Fe at 5.9 keV and 6.5 keV are partially absorbed by a thin silver foil mounted in front of the ^{55}Fe nuclide to produce fluorescence at 3.0 keV and 3.15 keV. The silver foil is 1.6 μm thick and is deposited between two polyimide foils which are 8 μm (on the side toward the ^{55}Fe) and 2 μm (on the opposite side). Photons at 3.0 keV and 5.9 keV, broadly collimated, are diffracted by a graphite mosaic crystal with FWHM mosaicity of 1.2 deg at first and second order of diffraction, approximately at the same diffraction angle (about 0°.5). A diaphragm is used to block the stray-light X-rays except scattered X-rays from the graphite.
5. Calibration source B (Cal B). This source produces a collimated beam of unpolarized photons to monitor the degree of spurious modulation. An ^{55}Fe radioactive source is glued in a holder and screwed in a cylindrical body. A diaphragm with an aperture of 1 mm collimates X-rays from the ^{55}Fe to produce a spot of about 3 mm on the GPD; such a spot has a size that is representative of the source image of a point-like source when the spacecraft dithering is included.
6. Calibration source C (Cal C). This source will illuminate the entire detector-sensitive area to map the gain at one energy. This source is composed of an ^{55}Fe radioactive source glued in a holder that is screwed in a body. A collimator allows
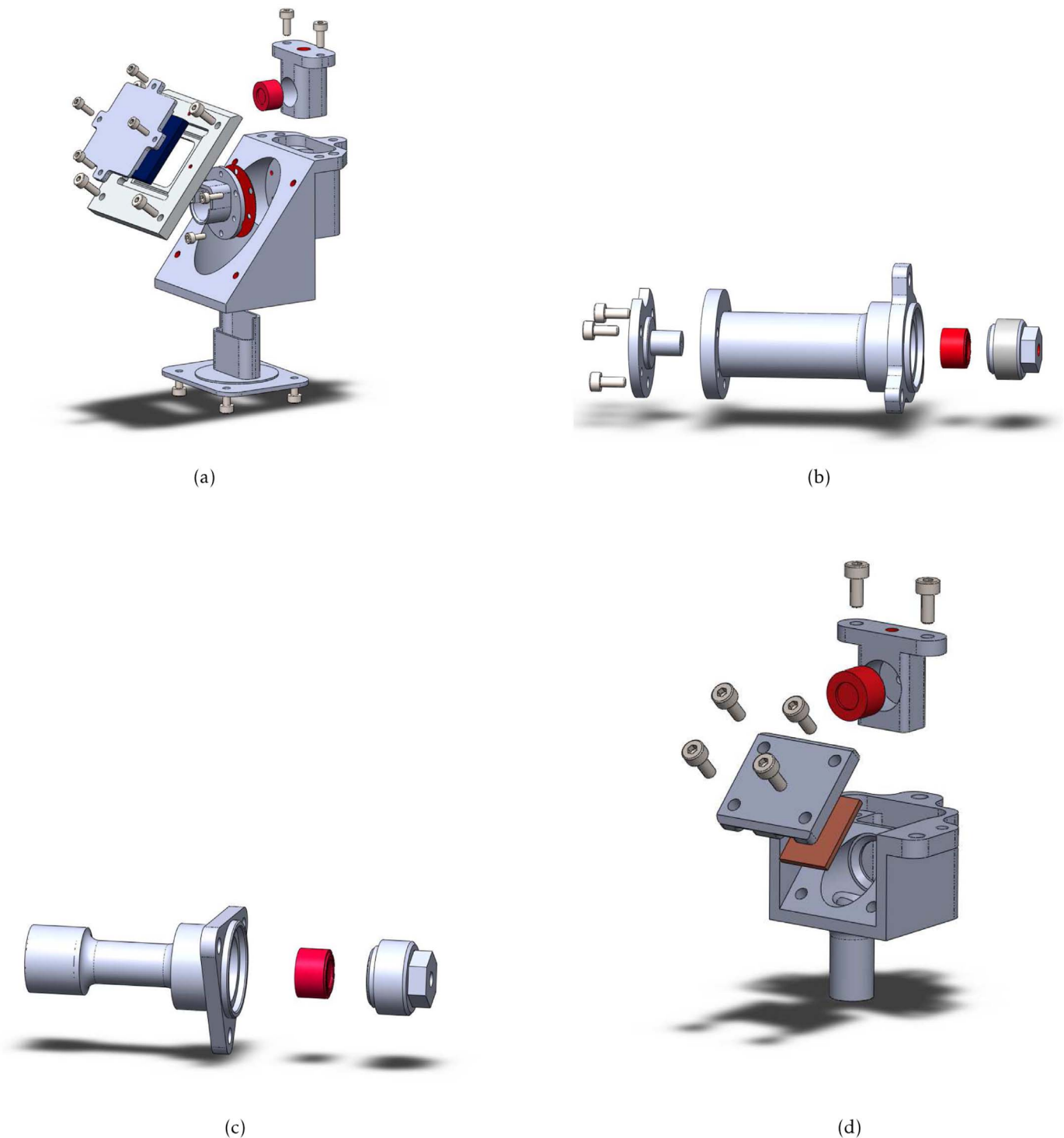
(a)

(b)

(c)

(d)

Figure 6. CAD models of the calibration set. All sources are derived from capsules containing an ^{55}Fe nuclide. (a) Cal A is the polarized source. It is un-collimated and provides simultaneous polarized X-rays at 3.0 keV and 5.9 keV. (b) Cal B is an unpolarized collimated 5.9 keV source. (c) Cal C is a broad 5.9 keV source for flat-field illumination. (d) Cal D is a broad 1.7 keV source for gain and spurious modulation check-out.

X-ray photons to impinge on the detector-sensitive area only when the source is in front of the GPD.

7. Calibration source D (Cal D). This source will illuminate the full detector-sensitive area like the Cal C, to map the gain at another energy. Cal D is based on an ^{55}Fe source, glued in an aluminum holder that illuminates a Si target mounted on a body to extract Kα fluorescence from silicon. This source produces fluorescence emission at 1.7 keV. Silicon would provide, together with Cal C, more *leverage* for gain-calibration and, since photoelectron tracks are smaller at this energy, the gain map can have a higher spatial resolution. It is worth noting that the design is such that X-ray photons from ^{55}Fe cannot directly impinge on the GPD sensitive area to avoid detector saturation. Moreover it allows for monitoring spurious modulation at low energies.
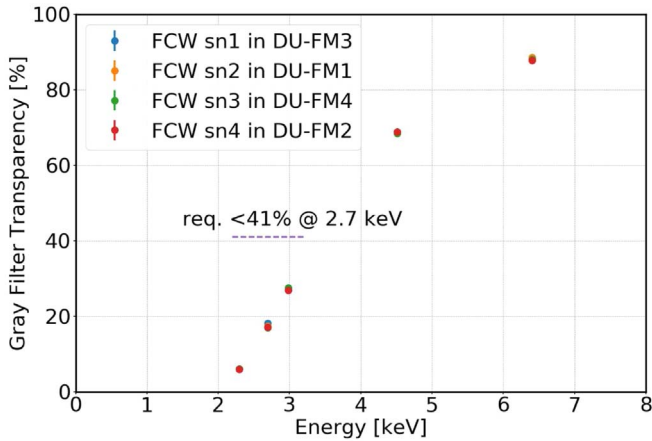
Figure 7. The measured transparency of the gray filter used in each DU.

Calibration Source	Activity (mCi)	Counting Rate (c/s)
Cal A	100	1.3 @ 3.0 keV
		15 @ 5.9 keV
Cal B	20	44 @ 5.9 keV
Cal C	0.5	98 @ 5.9 keV
Cal D	100	61 @ 1.7 keV

All calibration sources inside the FCW contain an ^{55}Fe nuclide whose activity naturally decays with a half-life of 2.7 yr. In Table 3 we report the expected flight rate at the beginning of the operative phase of IXPE which, at the time of this writing, is 2021 November.

Replacement/installation of the radioactive nuclide is possible through a dedicated opening in the DU lid. Radioactive sources, glued in their holders, can be extracted with dedicated tools and replaced with new ones in new holders.

8. Detector Service Unit

Thanks to the functionalities of the ASIC and of the GPD readout system, most of the necessary operations on the data are performed by the DAQ electronics (Barbanera et al. 2021) including acquisition, digitation of the pixel charge, zero-suppression, and efficient data packing. We designed the DSU in order to mainly perform data formatting in a way suitable for storing into the spacecraft memory (5 GByte) and for using the S band for downloading. The DSU also controls the filter and calibration wheels and manages the payload operative modes.

The DSU provides the following functions for the operation and autonomy of the IXPE instrument.

1. Power supply generation (secondary power to supply the DU's sub-units).
2. Telemetry management (data acquisition, formatting, and transmission to the S/C).
3. Commands management (reception, verification, generation, scheduling, distribution, or execution).
4. Time management (synchronization of the DUs, pulse-per-second (PPS) distribution, and time tagging).
5. Filter and calibration wheel management.
6. Science data management (retrieving, isolated pixels removal, formatting, and transmission to the S/C).
7. Payload mode control
8. GPD temperature control.
9. Fault detection isolation and recovery (FDIR) management.

The DSU consists of two boards with cold redundancy and one backplane for internal DSU signal routing. The boards are the single board computer (SBC) and the power and service board (PSB).

Figure 8 shows the high-level architecture of the DSU with its main electrical interfaces.

The SBC implements the instrument control and configuration and the instrument data processing and formatting. In fact, it performs a rejection of raw data called "orphan removal" (see Section 8.2). The SBC is based on a LEON3FT central processing unit (CPU). The LEON3FT CPU is implemented in ASIC provided by COBHAM (UT699). A companion field-programmable gate array (FPGA), belonging to the RTAX family by MICROSEMI, is included to support the processor operation and to provide the management of data interfaces required by the IXPE instrument and not included in the ASIC.

The PSB performs different tasks relevant to power management; in particular, this board hosts the power converters aimed at the generation of required supply voltages both for DU and DSU electronics. The drivers for DU thermal actuators (heaters and Peltier cells) and for the FCW are also installed. The DSU also implements signal conditioning for the resistance temperature detectors (RTD) of the DU temperature control and for the motor positioning sensors of the FCWs and their temperature.

DSU architecture supports a redundancy philosophy based on a cold-sparing approach. The only exception is the power I/F for each FCW motor that is equipped with a redundant coil for each motor phase. For each motor phase, the main coil is connected to the main PSB motor driver and the redundant coil to the redundant PSB motor driver. For this reason, one temperature sensor is connected to the main PSB and the other one to the redundant PSB.

The data interface between DSU and each DU consists of the following five sets of three signal lines which comply with the low-voltage differential signal (LVDS) standard:

1. Three command and communication interfaces (CCI) for command transmission from DSU to each DU.
2. Three serial data interfaces (SDI) for sensor data transmission from each DU to DSU.
3. Three reset lines, one for each DU.
4. Three input alarm lines, one for each DU, used to switch off the relevant DU in case of an anomaly detected by the BEE.
5. Three output timing signals for DU internal acquisition timing verification.

IXPE uses a centralized spacecraft memory bank for data storage and transmission. The memories onboard the DSU are used only to store the boot SW and support the CPU and FPGA operation.

The local bus connects the LEON3FT CPU, the FPGA, the central SRAM (static random access memory), the PROM (programmable read-only memory) and MRAM (magnetoresistive random access memory). In order to minimize bus loading, the MRAM is connected to the local bus via bus
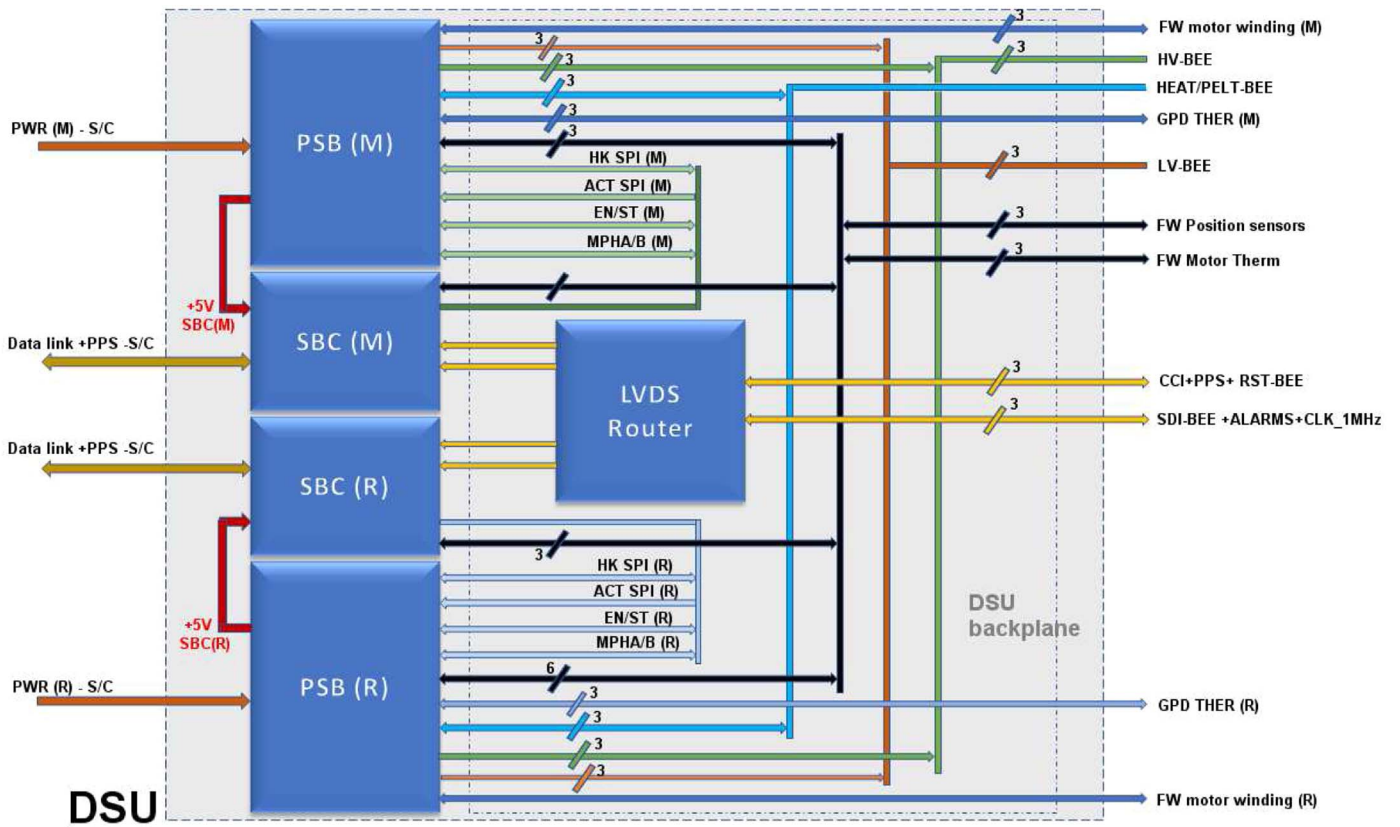
Figure 8. DSU high-level architecture.

switches. After boot-phase completion, the MRAM is disconnected from the bus.

The DSU interfaces the spacecraft with two (one nominal and one redundant) unregulated power lines on separate connectors. The nominal voltage of the power lines is 28 V. Minimum and maximum values of input power provided by S/C are, respectively, 26 V and 34 V.

8.1. IXPE Instrument Timing Architecture

The IXPE satellite manages the timing of the events using a GPS receiver. The GPS provides a PPS received by the instrument through a dedicated line. The spacecraft also provides the time of day (TOD) with a frequency of 1 Hz. The TOD contains information about the validity of the previously provided PPS and the time of the next PPS. A plot showing the timing scheme is shown in Figure 9.

The DSU is equipped with a temperature-compensated crystal oscillator (TCXO) with an accuracy <4 ppm. The PPS and the 1 MHz clock generated by the 1 MHz local oscillator are provided to each DU.

The onboard time (OBT) management is based on a master OBT implemented in the DSU and 3 local OBTs implemented in the DUs. The master OBT and the locals OBTs are composed of (i) a 29 bit counter for the seconds (>16 yr of mission lifetime) and (ii) a 20 bit counter for the microseconds (1 μs resolution) and a register for the OBT error (error counter).

At boot, the master OBT is initialized by subtracting the start mission date (stored in the DSU MRAM) from the GPS time.

During nominal observation, when the GPS is valid, the second counter is incremented upon receiving the PPS and the microsecond counter is incremented by the 1 MHz local
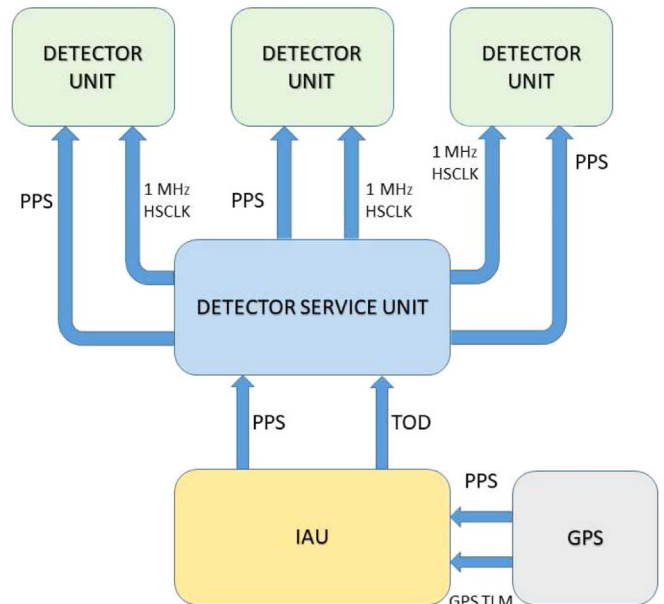

Figure 9. The architecture of timing for the instrument.

oscillator. At the arrival of the PPS, the difference of the microsecond counter with respect to 10^6 is stored in the Master OBT error counter and included in the housekeeping packet data with 1 μs resolution and 1 s rate. The local OBTs are updated in the same way by the FPGA located in the BEE using the PPS provided by the S/C through the DSU and the 1MHz clock provided by the DSU.
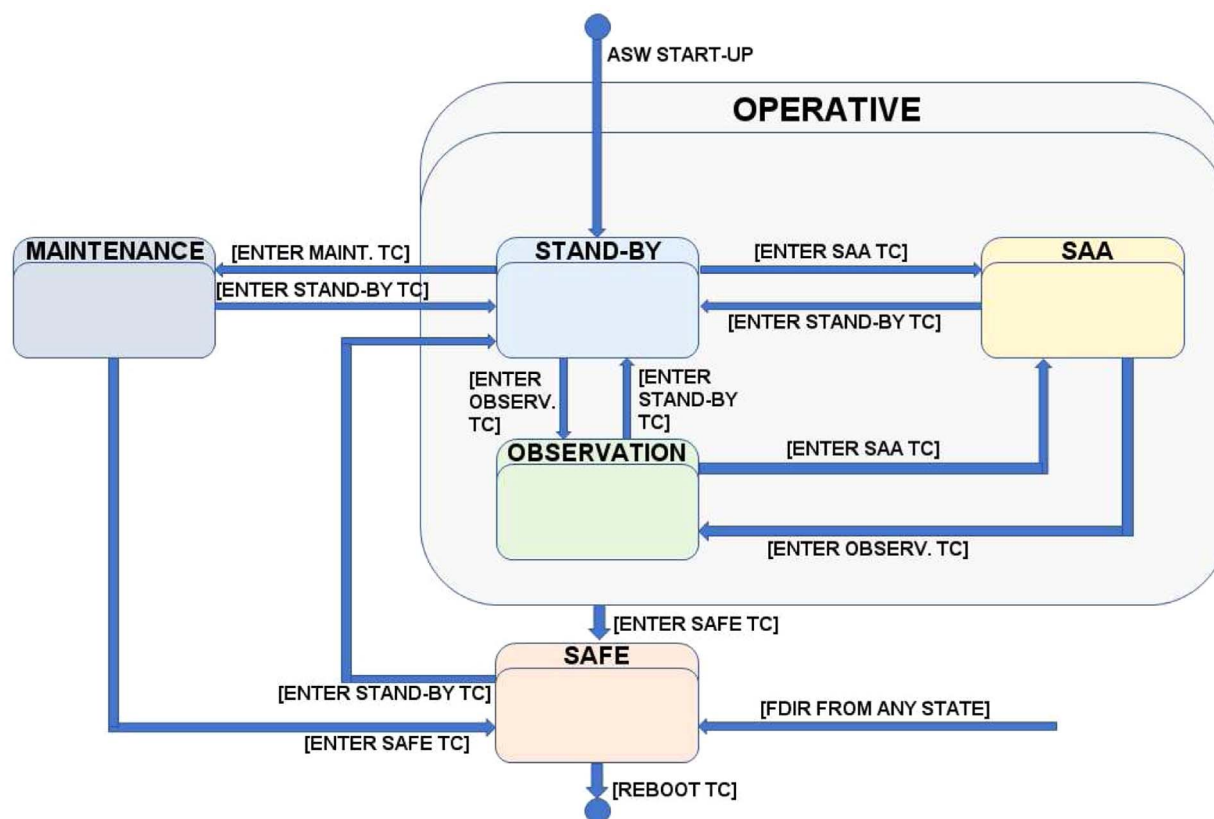
Figure 10. The operative modes of IXPE payload and the transition via telecommand and FDIR.

If the previous PPS is not valid, as indicated by the TOD, the PPS provided by the S/C is not used. The DSU synthesizes the PPS for the DUs using the local TCXO. During this operation mode, the OBT error is set equal to zero. The nonvalid condition information is included in the housekeeping (HK) data. The master OBT remains in free running until the reception of the sequence of TOD reporting that the PPS is newly valid. In this case the DSU re-initializes the instrument timing as at instrument boot.

The alignment of the local OBT with the master OBT is verified using the housekeeping telemetry (TM). The HK telemetry (TM) comprises the values of the locals OBT and the master OBT every second. At the MOC/SOC, these values are monitored and in case of misalignment, an action recovery is planned (e.g., time reset by telecommand).

8.2. Orphan Removal of Data

The fulfillment of the requirement on the maximum counting rate is possible thanks to the DAQ that packs consecutive zeros by writing their number in a single word (Barbanera et al. 2021) and the isolated pixel removal in the DSU. As a matter of fact, the only data processing made onboard by the DSU is the removal of isolated pixels (called *orphans* in the photoelectron track image) generated by noise. This removal is performed with a simple algorithm on the serial stream of the zero-suppressed data delivered by the DU for each event. It requires a limited memory allocation and is performed by the FPGA without impact on the CPU timing. By means of the packing in the DU and the removal of isolated pixel it is possible to reduce the data rate within the requirements for the S band. In fact,

only the pixels that identify the tracks are downloaded, suppressing the isolated pixel generated by noise.

8.3. Instrument Operative Mode Specifications and Transitions

The instrument operative modes are managed by the DSU and they are selected either via telecommand or by activating autonomously an FDIR procedure. The BEE is controlled by the DSU and if it generates an alarm condition, the DSU responds by setting the instrument in safe mode. The transition between modes is described by Figure 10.

The foreseen payload operative modes are the following.

1. Boot (transitional mode). BOOT is the start-up mode at power on. A limited SW application, called Boot Software, runs from the programmable read-only memory (PROM) in order to perform all the checks and the initialization of instrument resources and items. In the nominal case, the application software (ASW) completes the initialization sequence execution by placing the instrument in STAND-BY. The boot phase lasts around 60 s.

2. Maintenance. This mode is reserved to support the in-orbit maintenance program. This mode can be reached on request when the DSU SW mode is in stand-by and is dedicated to memory management operations like code and data load/download in/from MRAM and SRAM.

3. Stand-by. Nominally, at the end of the boot-strap phase, the DSU moves into stand-by mode to start the instrument monitoring and control. The stand-by mode supports the starting and handling of the thermal regulation, powering on and off the instrument items,

the processing of the incoming telecommands, and the generation of the related TM. Finally, it configures the detector units and the science data processing.

4. Observation. From the point of view of the DSU, all instrument calibration and scientific modes are managed into a unique Observation mode that is preventively configured while in Stand-by mode. This mode supports the handling of thermal regulation, the handling of the time-of-day message, the collection of the housekeeping, and the generation of scientific data.

5. South Atlantic Anomaly (SAA). This mode is used when the satellite crosses the South Atlantic Anomaly which happens once per orbit. In this mode, the high voltage (HV) is ramped down below the voltage that sets multiplication; the science data generation is disabled while housekeeping data are generated and collected as usual.

6. Safe. This mode is used before switching off the instrument or performing an SW reboot and managing the FDIR conditions. This mode preserves DU and HV status (i.e., no ramp off or switch off is performed on hardware) when entered by telecommand. If entered by FDIR, HVs ramp off, DUs switch off, and FCW rotation to CLOSE can be performed as part of the *Recovery* action. In this operative mode, the instrument generates and collects the housekeeping. It is possible to perform a reboot of the ASW only during Safe mode.

7. Reboot (transitional mode). At the DSU switch-on, after the BOOT SW activities the ASW are loaded into SRAM and executed, the ASW checks the position of the filters and calibration wheels and the status of the detector units and high-voltage boards.

   If the FCWs are closed and the HVBs are off, the ASW moves to STAND-BY mode. If the FCWs are not closed or if the HVBs are ON, the ASW moves the FCWs to the CLOSED position, performs the ramp-off procedure if HVBs voltages are greater than zero, switches off the DUs, and moves SW operative mode to Safe.

9. The Calibration of the IXPE Detector Units

Being a discovery mission, celestial sources are not available for performing in-flight calibration for polarimetry. In fact, the measurement performed 45 yr ago on the Crab Nebula (Weisskopf et al. 1978b) with a nonimaging detector, cannot be used as a "flight" calibrator. Indeed, this time interval is already about 5% of its lifetime and the Crab Nebula was found to vary. For these reasons, an on-ground detailed calibration is mandatory.

Furthermore, we designed and built an onboard calibration system aimed at checking variations in the modulation factor even if not with the same accuracy reached on ground, and any variation on spurious modulation (see Section 7.2).

The calibration of the detector units is a key activity for IXPE. Details of the calibration facility and of the calibration results will be presented in forthcoming papers. Beside validating the Monte Carlo prediction for the modulation factor, more importantly, it provides physical parameters like (i) the low-energy spurious modulation which is the instrument response to unpolarized radiation (see Section 6.2 and Figure 12) and (ii) the gain nonuniformities that cannot be modeled in advance: they have been calibrated on ground and

included in the data-processing pipeline. The calibration strategy mimics the observation strategy during flight that foresees dithering of point sources. In this way, when we calibrated the entire detector, we obtained the so-called flat-field (FF) measurements. When we calibrated at high count rate density, only a selected central part of the detector active region, we obtained the so-called deep flat-field (DFF) measurements. The latter are aimed at reaching very large statistics within the dithering region foreseen in flight for point-like celestial sources. When we calibrated with a narrow beam (less than 1 mm diameter), we obtained the so-called "spot measurements."

The calibration activity (40 days for each DU) was directed toward measuring the following physical quantities:

1. Spurious modulation (60% of the calibration time) at six energies between 2 keV and 5.9 keV in a DFF configuration (central region with 3.25 mm diameter at a density of 10^6 counts mm^{-2}) and FF configuration (all detector-sensitive area with 10^5 c mm^{-2}).

2. Modulation factor (17.5% of the calibration time) at seven energies, and different polarization angles, between 2.0 keV and 6.4 keV in DFF configuration (3.25 mm radius, 10^4 counts mm^{-2}) and in FF configuration (7 mm radius with the same statistics of DFF but in a larger area).

3. Efficiency at three or more energies (2.5% of the calibration time).

4. Spatial resolution (2.5% of the calibration time) of unpolarized radiation at three energies in an array of 3×3 spots.

5. Spatial resolution (2.5% of the calibration time) of polarized radiation at three energies in one point.

6. Gray filter transparency at five energies, inclined penetration (focusing effect), and calibration of the FCW sources (the rest of the fractional time).

From the above measurements, it was also possible to derive the following physical quantities.

1. Accuracy of the polarization angle measurement at seven energies.

2. Map of the gain variations in the active region.

3. Measurement of the energy resolution at different energies.

4. Measurement of the dead time at different energies.

We measured the modulation factor at different angles not only to measure the accuracy of the polarization angle but also to check that spurious modulation is properly subtracted. Indeed, any change of the modulation factor with polarization position angle is expected in the presence of spurious effects, which mimic the presence of a secondary, albeit small, polarization component.

We organized the calibration in such a way that the time dedicated to measuring spurious modulation at different energies accounts for 60% of the total calibration time. As a matter of fact, in order to measure spurious modulation at a level of 0.1% across the sensitive area, we collected tens of millions of counts for each energy. The calibration time was set considering the maximum counting rate allowed for the DUs due to their dead time and the power of the X-ray tubes.

In order to perform such calibrations we built two stations. One station is the main calibration station (called ICE, instrument calibration equipment). The other, called AIV/T
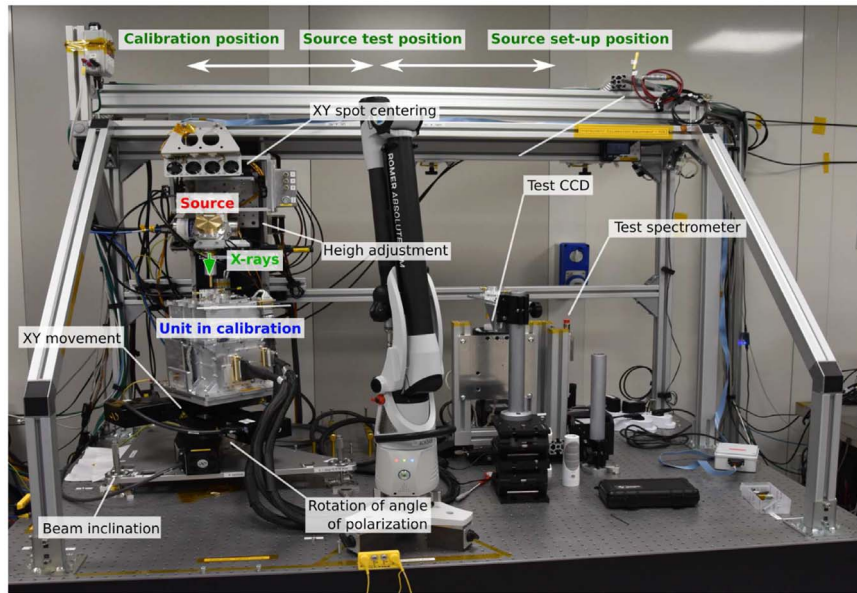
Figure 11. The instrument calibration equipment at INAF-IAPS. On the left is a flight DU under calibration with a polarized source. At the center, the Romer arm used for metrology is visible. On the right, the CCD used to study the beam image and the SDD used to study the beam spectrum are just visible.

Table 4
The Crystals and the X-Ray Tubes Used during GPD Acceptance and DU Calibration

Crystal	X-ray tube	Energy (keV)	2D (Å)	Diffraction Angle (deg)	$\frac{R_p}{R_s}$	Polarization (%)
PET (002)	Continuum	2.01	8.742	45.0	0.0	$\approx$100.0
InSb (111)	Mo L_α	2.29	7.481	46.361	0.0034	99.2%
Ge (111)	Rh L_α	2.7	6.532	44.877	0.00	$\approx$100.0
Si (111)	Ag L_α	2.98	6.271	41.562	0.0252	95.1%
Al (111)	Ca K_α	3.69	4.678	45.909	0.0031	99.4%
Si (220)	Ti K_α	4.51	3.840	45.716	0.0023	99.5%
Si (400)	Fe K_α	6.40	2.716	45.511		$\sim$100%

Note. This is a subset of available energies. The column $\frac{R_p}{R_s}$ represents the ratio of the integrated reflectivity for polarization parallel and perpendicular to the crystal lattice plane at that given energy. From this ratio it is possible to derive the polarization degree of the reflected beam (from Henke et al. 1993).

calibration equipment (ACE) is designed to illuminate contemporaneously up to three DUs to support the integration and test of the whole instrument, but it can host the same calibration sources as the main station. During some periods, ACE was indeed used to carry out calibration measurements in parallel with ICE. They are the so-called AIV &T calibration equipment (ACE1 and ACE2).

The ICE is derived from an earlier design that was used for 15 yr at INAF-IAPS (Muleri et al. 2008b, 2021). In particular, it includes.

1. The X-ray sources used for calibration and functional tests. Each source emits X-ray photons at known energy and with a known polarization degree and angle. Polarized sources exploit Bragg diffraction at nearly 45° from a set of crystals (see Table 4) with suitable X-ray tubes. Unpolarized sources are based on direct emission from X-ray tubes or on the extraction of fluorescence emission from a target. The direction of the beam, the position angle for polarized sources, and its position can be measured with respect to the GPD thanks to its fiducial points and the use of a Romer measurement arm.

2. The test detectors, one commercial silicon drift detector (SDD) by AMPTEK and one X-ray CCD camera by Andor. They are used to characterize the beam before DU calibration and as a reference for specific measurements (e.g., the measurement of quantum efficiency with the SDD).

3. All the electrical and mechanical equipment required to support the DU and the calibration sources, monitor the relevant diagnostic parameters, and assure safety during calibrations.

The ICE in the configuration with the polarized source is shown in Figure 11. The DU is mounted in the ICE without the stray-light collimator and the UV filter. In this way, we minimize the distance between the X-ray source and the GPD and hence air absorption and beam divergence. The DU is placed on the top of a tower that allows one to do the following.

1. Move the DU on the plane orthogonal to the incident beam with an accuracy of ± 2 μm (over a range of 100 mm) to map the GPD sensitive surface.

2. Rotate the DU on the plane orthogonal to the incident beam with an accuracy of $\pm 7''$ to test the response at
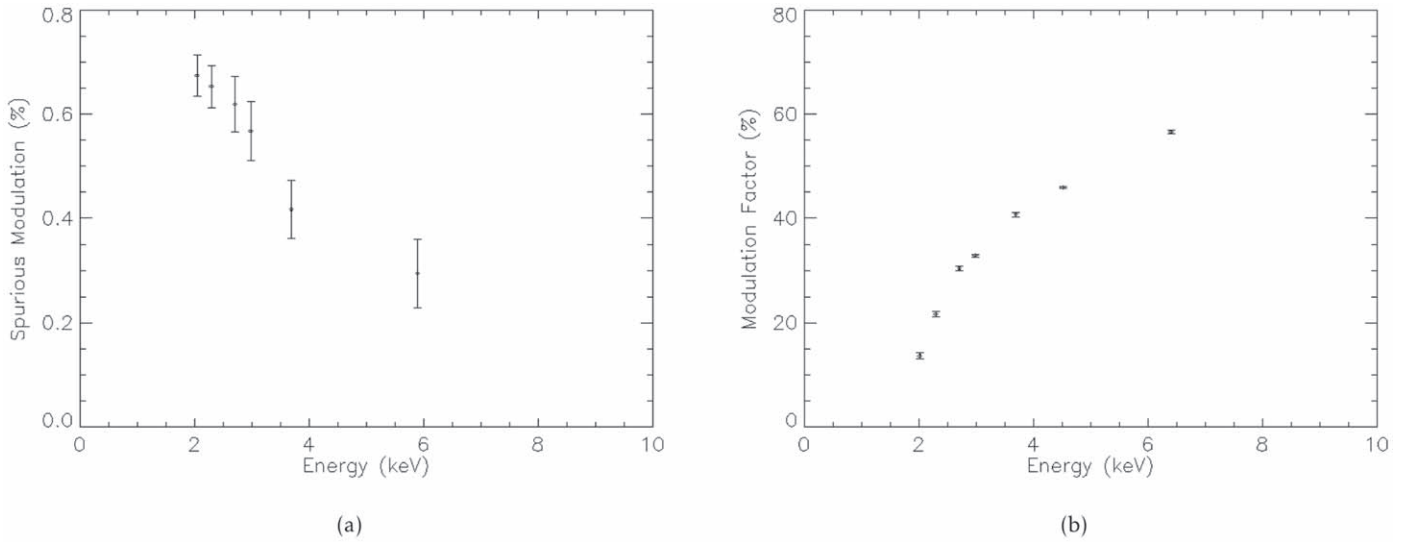
Figure 12. a) Spurious modulation at instrument level (on a spot of 1.5 mm radius and combining the three DUs clocked at 120°). (b) Modulation factor of the instrument after spurious modulation subtraction (average of the three DUs), with dithering on a flight-representative region of 1.5 mm radius.

Table 5
Instrument Performance

Parameter	2.69 keV	6.40 keV
Modulation factor	30.4% ± 0.4%	56.6% ± 0.4%
Efficiency (expected during flight)	13.5%	1.7%
Gray filter transparency	17.4%	88.0%
UV Filter transparency	(95.94 ± 0.26)%	(99.44 ± 0.38)%
Spurious modulation	(0.62 ± 0.05)%	(0.29 ± 0.06)% (@5.89 keV)
Systematic error on the PA determination	(0.143 ± 0.094)°	(0.186 ± 0.097)°
Energy resolution	(22.2 ± 0.5)%	(16.3 ± 0.1)%
Position resolution (HPD)	(118.7 ± 5.2) μm	120.0 ± 5.8) μm
Dead time	1.1 ms	1.2 ms

Parameter	Value
Timing accuracy	1–2 μs (by means of the use of the PPS)
Timing resolution	1 μs
Common FoV	9′
Dithering radius	1′.6 standard (or 0′.8 or 2′.6 or no-dithering)
Expected background rate (2–8 keV)	1.9 10^{-3} c/s/cm^2/keV
Expected Crab (nebula + pulsar)[a] rate (2–8 keV)	150 c/s
Expected Crab (nebula + pulsar) rate (1–12 keV)	240 c/s

Notes. Spurious modulation is effectively measured at instrument level, thus considering 120° clocking of three DUs. Data are extracted in a circular region of 1.5 mm radius. Efficiency includes only the GPD contribution extrapolated at the time of the flight.
[a] Crab spectrum as in Zombeck (2007).

different polarization angles and to average residual polarization of unpolarized sources, if necessary.

3. Tip/tilt align the orthogonal direction of the GPD to the incident beam. Two out of the three feet of the tip/tilt plate are manual micrometers, but one is motorized to carry out automatic measurements with the beam off-axis of a series of known angles, between <1° and about 5°, e.g., to simulate the focusing of X-ray mirror shells.

The calibration of the flight DUs was performed successfully following the on-ground calibration plan. The major effort was the calibration of the modulation factor and the characterization and the subtraction of spurious modulation at different energies. The detailed description of these features is the subject of forthcoming papers.

10. Instrument Performance

We summarize here the instrument performance after calibration. We show in Figure 12 the results for spurious modulation and modulation factor. In the left panel we show spurious modulation re-phasing the modulation curves when considering dispositions of the DUs as in flight (120° clocking around Z axis). The orientation of the DUs allows for reducing the spurious modulation of the instrument with respect to that of a single DU. Such spurious modulation is subtracted on an event-by-event basis. The right plot shows, instead, the modulation factor after keeping 80% of the data among the most elongated track and event-by-event spurious modulation subtraction.

In Table 5 we show the characteristics of the instrument as an average of the three DUs at two characteristic energies.

These parameters can be considered as representative of the entire instrument. The detailed calibration results for each flight DU will be presented in a set of forthcoming papers.

11. Processing Pipeline

Data are analyzed on ground. The first step of the pipeline is to convert binary telemetry files to FITS standard format by means of a parser. At this stage, data contain all the information provided by the instrument and the relevant information from the spacecraft. In particular they contain the raw, pedestal-corrected, tracked images, the time of each count, and all the relevant housekeeping such as temperatures and event-by-event dead time. The FITS-converted data are then processed in order to transform the engineering unit in physical units, removing the unnecessary engineering information and including good time interval information. The processing pipeline, then, uses calibration data in order to (1) equalize the pixel response of the track image; (2) identify by means of a clustering algorithm the photoelectron (principal) track; (3) estimate the emission direction in detector coordinates; (4) estimate the location of the events in detector coordinates; (5) estimate the energy of the track by applying (a) correction for charging, (b) correction for temperature, and (c) GEM gain nonuniformities. The last step of the correction is the removal of spurious modulation, which is applied on the Stokes parameter calculated for each event. At this stage, track images are removed and data contain the position in detector coordinates, the time of the event, the energy of the event in "pulse invariant" unit, the emission direction in detector coordinates and the Stokes parameter of the event according to Kislat et al. (2015) definition with only an extra factor of two. The next step is to merge the detector data from the three DUs, including their clocking at 120°, and to convert them to celestial coordinates. The final event file to be used for science analysis, after all the procedures are applied, contains all the information typical of an imaging X-ray astronomy mission, but with the addition of the information on the emission direction of the photoelectron in celestial coordinates.

12. Conclusion

We presented the instrument which was successfully designed, built, calibrated, and installed on the spacecraft for the IXPE mission. These activities spanned 3.5 yr, including phase B, and the development time is compliant with readiness for a launch starting 2021 December 7. We reviewed the instrument design and the results of the calibration and we compared them with those expected on the basis of scientific astrophysical requirements. The modulation factor, the energy resolution, and the position resolution of the instrument all meet the scientific requirements. The quantum efficiency is below requirement, but when factoring in all other parameters, the top-level polarization sensitivity requirement is still met. Background also is expected to be slightly higher than the requirement (Xie et al. 2021). However, due to the relatively bright sources in the IXPE observing plan, we anticipate no effect in point-like source observation and only a mild effect is expected in low-surface-brightness extended sources like the molecular clouds in the vicinity of the Galactic Center or in the SN1006 supernova remnant. The calibration of the spare telescope, the only one to be calibrated, has been accomplished and its results will be part of a forthcoming paper. The preliminary results are such that in-flight performance of the IXPE payload will permit a new window to be opened in X-ray polarimetry.

ORCID iDs

Paolo Soffitta https://orcid.org/0000-0002-7781-4104
Luca Baldini https://orcid.org/0000-0002-9785-7726
Ronaldo Bellazzini https://orcid.org/0000-0002-2469-7063
Enrico Costa https://orcid.org/0000-0003-4925-8523
Luca Latronico https://orcid.org/0000-0002-0984-1856
Fabio Muleri https://orcid.org/0000-0003-3331-3794
Ettore Del Monte https://orcid.org/0000-0002-3013-6334
Sergio Fabiani https://orcid.org/0000-0003-1533-0283
Carmelo Sgro' https://orcid.org/0000-0001-5676-6214
Fabrizio Amici https://orcid.org/0000-0002-2637-8971
Matteo Bachetti https://orcid.org/0000-0002-4576-9337
Rita Carpentiero https://orcid.org/0000-0002-7723-8135
Marco Castronuovo https://orcid.org/0000-0002-6103-332X
Stefano Ciprini https://orcid.org/0000-0002-0712-2479
Alessandro Di Marco https://orcid.org/0000-0003-0331-3259
Riccardo Ferrazzoli https://orcid.org/0000-0003-1074-8605
Fabio La Monaca https://orcid.org/0000-0001-8916-4156
Simone Maldera https://orcid.org/0000-0002-0698-4421
Alberto Manfreda https://orcid.org/0000-0002-0998-4953
Giorgio Matt https://orcid.org/0000-0002-2152-0916
Alessio Nuti https://orcid.org/0000-0002-9352-2355
Matteo Perri https://orcid.org/0000-0003-3613-4409
Melissa Pesce-Rollins https://orcid.org/0000-0003-1790-8018
Raffaele Piazzolla https://orcid.org/0000-0002-4222-6919
Maura Pilia https://orcid.org/0000-0001-7397-8091
John Rankin https://orcid.org/0000-0002-9774-0560

References

Angel, J. R., Novick, R., vanden Bout, P., & Wolff, R. 1969, PhRvL, 22, 861
Baldini, L., Barbanera, M., Bellazzini, R., et al. 2021, APh, 133, 102628
Barbanera, M., Citraro, S., Magazzu', C., et al. 2021, ITNS, 68, 1144
Bellazzini, R., Spandre, G., Minuti, M., et al. 2006, NIMPA, 566, 552
Bellazzini, R., Spandre, G., Minuti, M., et al. 2007, NIMPA, 579, 853
Black, J. K., Baker, R. G., Deines-Jones, P., Hill, J. E., & Jahoda, K. 2007, NIMPA, 581, 755
Connors, P. A., & Stark, R. F. 1977, Natur, 269, 128
Costa, E., Soffitta, P., Bellazzini, R., et al. 2001, Natur, 411, 662
Elsner, R. F., O'Dell, S. L., & Weisskopf, M. C. 2012, Proc. SPIE, 8443, 84434N
Fabiani, S., Costa, E., Del Monte, E., et al. 2014, ApJS, 212, 25
Feng, H., Li, H., Long, X., et al. 2020, NatAs, 4, 511
Ferrazzoli, R., Muleri, F., Lefevre, C., et al. 2020, JATIS, 6, 048002
Heitler, W. 1954, Quantum Theory of Radiation (3rd ed.; Oxford: Clarendon)

Henke, B. L., Gullikson, E. M., & Davis, J. C. 1993, ADNDT, 54, 181
Hughes, J. P., Long, K. S., & Novick, R. 1984, ApJ, 280, 255
Kaaret, P., Novick, R., Martin, C., et al. 1989, Proc. SPIE, 1160, 587
Kislat, F., Clark, B., Beilicke, M., & Krawczynski, H. 2015, APh, 68, 45
La Monaca, F., Fabiani, S., Lefevre, C., et al. 2021, Proc. SPIE, 11444, 1029
Muleri, F., Piazzolla, R., Di Marco, A., et al. 2021, APh, in press
Muleri, F., Soffitta, P., Baldini, L., et al. 2008a, NIMPA, 584, 149
Muleri, F., Soffitta, P., Baldini, L., et al. 2010, NIMPA, 620, 285
Muleri, F., Soffitta, P., Bellazzini, R., et al. 2008b, Proc. SPIE, 7011, 701127
Novick, R., Weisskopf, M. C., Berthelsdorf, R., Linke, R., & Wolff, R. S.
    1972, ApJL, 174, L1
O'Dell, S. L., Attinà, P., Baldini, L., et al. 2019, Proc. SPIE, 11118, 111180V
O'Dell, S. L., Baldini, L., Bellazzini, R., et al. 2018, Proc. SPIE, 10699, 106991X
Ramsey, B. D., Bongiorno, S. D., Kolodziejczak, J. J., et al. 2019, Proc. SPIE,
    11119, 1111903
Sanford, P. W., Cruise, A. M., & Culhane, J. L. 1970, in Non-Solar X- and
    Gamma-Ray Astronomy, Vol. 37 ed. L. Gratton, 35
Schnopper, H. W., & Kalata, K. 1969, AJ, 74, 854
Soffitta, P., Attinà, P., Baldini, L., et al. 2020, Proc. SPIE, 11444, 1144462
Soffitta, P., Barcons, X., Bellazzini, R., et al. 2013a, ExA, 36, 523
Soffitta, P., Campana, R., Costa, E., et al. 2012, Proc. SPIE, 8443, 84434N
Soffitta, P., Costa, E., di Persio, G., et al. 2001, NIMPA, 469, 164
Soffitta, P., Costa, E., Kaaret, P., et al. 1998, NIMPA, 414, 218
Soffitta, P., Muleri, F., Fabiani, S., et al. 2013b, NIMPA, 700, 99
Soffitta, P. & XIPE Collaboration 2017, NIMPA, 873, 21
Stark, R. F., & Connors, P. A. 1977, Natur, 266, 429
Swank, J. 2010, in X-ray Polarimetry: A New Window in Astrophysics, ed.
    R. Bellazzini et al. (Cambridge: Cambridge Univ. Press), 251
Tamagawa, T., Hayato, A., Asami, F., et al. 2009, NIMPA, 608, 390
Tamagawa, T., Hayato, A., Iwahashi, T., Konami, S., Fumi, A., et al. 2010, in
    X-ray Polarimetry: A New Window in Astrophysics, ed. R. Bellazzini et al.
    (Cambridge: Cambridge Univ. Press), 251
Tomsick, J., Costa, E., Dwyer, J., et al. 1997, Proc. SPIE, 3114, 373
Weisskopf, M. C., Bellazzini, R., Costa, E., et al. 2008, Proc. SPIE, 7011,
    70111I
Weisskopf, M. C., Kestenbaum, H. L., Long, K. S., Novick, R., & Silver, E. H.
    1978a, ApJL, 221, L13
Weisskopf, M. C., Ramsey, B., O'Dell, S., et al. 2016, Proc. SPIE, 9905,
    990517
Weisskopf, M. C., Silver, E. H., Kestenbaum, H. L., et al. 1977, ApJL,
    215, L65
Weisskopf, M. C., Silver, E. H., Kestenbaum, H. L., Long, K. S., & Novick, R.
    1978b, ApJL, 220, L117
Xie, F., Ferrazzoli, R., Soffitta, P., et al. 2021, APh, 128, 102566
Zombeck, M. 2007, Handbook of Space Astronomy and Astrophysics: Third
    Edition (Cambridge: Cambridge Univ. Press)